Research Article

Teng Huang, Dongdong Zhang*, Yaxin Huang, Chengfei Fan, Yuan Lin, and Fukai Zhang

Flexural bearing capacity and failure mechanism of CFRP-aluminum laminate beam with double-channel cross-section

https://doi.org/10.1515/secm-2021-0012
Received Nov 25, 2020; accepted Feb 26, 2021

Abstract: In this study, the flexural bearing capacity and failure mechanism of carbon fiber-reinforced aluminum laminate (CARALL) beams with a double-channel cross-section and a 3/2 laminated configuration were experimentally and numerically studied. Two types of specimens using different carbon fiber layup configurations ($[0°/90°/0°]_3$ and $[45°/0°/-45°]_3$) were fabricated using the pressure molding thermal curing forming process. The double-channel CARALL beams were subjected to static three-point bending tests to determine their failure behaviors in terms of ultimate bearing capacity and failure modes. Owing to the shortcomings of the two-dimensional Hashin failure criterion, the user-defined FORTRAN subroutine VUMAT suitable for the ABAQUS/Explicit solver and an analysis algorithm were established to obtain a progressive damage prediction of the CFRP layer using the three-dimensional Hashin failure criterion. Various failure behaviors and mechanisms of the CARALL beams were numerically analyzed. The results indicated that the numerical simulation was consistent with the experimental results for the ultimate bearing capacity and final failure modes, and the failure process of the double-channel CARALL beams could be revealed. The ultimate failure modes of both types of double-channel CARALL beams were local buckling deformation at the intersection of the upper flange and web near the concentrated loading position, which was mainly caused by the delamination failure among different unidirectional plates, tension and compression failure of the matrix, and shear failure of the fiber layers. The ability of each fiber layer to resist damage decreased in the order of 90° fiber layer > 0° fiber layer > 45° fiber layer. Thus, it is suggested that 90°, 0°, and 45° fiber layers should be stacked for double-channel CARALL beams.

Keywords: Carbon fiber-reinforced aluminum laminates (CARALL); Channel cross-sectional beam; Flexural bearing capacity; Failure mechanism; Progressive failure analysis

1 Introduction

The application of new composite materials is a favorable way to reduce the weight and increase the span and bearing capacity of decomposable truss bridges [1–4]. Carbon fiber-reinforced polymer (CFRP) composites have the advantages of a low weight, high strength, corrosion resistance, and good design ability, thus significantly improving the bearing performance of load-bearing profiles. However, owing to their high cost, poor shear performance, and poor impact resistance of the resin matrix, these new composite materials are not widely used in civil engineering. If the new CFRP and conventional metal materials are combined in a composite component, their material deficiencies can be compensated for, and excellent comprehensive performance can be obtained. Fiber-reinforced metal laminates (FMLs) are a new type of composite material laminated by layers of metal and fiber-reinforced resin matrix composites in accordance with certain layup structure rules, and the layers are closely combined with each other. FMLs exhibit relatively low density, high strength, high ductility, and outstanding fatigue resistance, and have been widely used in aircraft manufacturing [5–7].

As a typical FML, the carbon fiber-reinforced aluminum laminate (CARALL) is laminated by alternately stacking CFRP prepregs and aluminum alloy sheets through adhesives. Its light weight and high strength are the main reasons why it has become a substitute for traditional structural materials. At present, extensive and detailed

***Corresponding Author: Dongdong Zhang:** College of Field Engineering, Army Engineering University of PLA, Nanjing 210007, China; Email: zhangdodo_163@163.com
Teng Huang, Yaxin Huang, Fukai Zhang: College of Field Engineering, Army Engineering University of PLA, Nanjing 210007, China
Chengfei Fan: Institute of Defense Engineering, AMS, PLA, Beijing 100850, China
Yuan Lin: State Key Laboratory of Disaster Prevention and Mitigation of Explosion and Impact, Army Engineering University of PLA, Nanjing 210007, China

researches have been conducted on the basic mechanical properties of CARALL, such as the in-plane and out-of-plane bending properties, progressive damage failure behavior and its affecting factors, and fiber layup optimization methods [8–17]. In addition, some studies have focused on the tensile properties of CARALL and the influence of the orifice stress concentration on the tensile properties [18–22]. There also exist many research reports on the delamination damage evolution mechanism [23–25], modal analysis using higher-order theories [26–28], fatigue properties [29–32], and impact and post-impact bearing performance of CARALL [33–40].

Owing to its outstanding characteristics, such as low weight, high strength, high ductility, and high impact resistance, CARALL demonstrates broad application potential in the development of dismountable bridges. Decomposable truss bridges consist of beams and columns with a variety of special-shaped cross-sections, such as box, I-shaped, single-channel, and double-channel cross-sections [1]. However, the existing research on FMLs mainly focuses on regular cross-sectional profiles [4–38], and existing studies on the related research and engineering applications of special-shaped cross-section members, particularly the double-channel cross-section, are limited [41, 42]. Therefore, it is necessary to study the load-bearing performance and failure mechanism of CARALL with a special-shaped cross-section, which would promote its application in large-span decomposable truss bridges.

In this study, a CARALL beam with a double-channel cross-section and a 3/2 laminated configuration was considered as the research object, and its flexural bearing capacity and failure mechanism were studied by a combination of experimental and numerical analyses. Two sets of double-channel cross-sectional laminated beams with carbon fiber layups of $[0°/90°/0°]_3$ and $[45°/0°/-45°]_3$ were prepared using compression molding and thermosetting forming processes. Three-point bending tests of the specimen were conducted to determine the ultimate bearing capacity and failure modes. In addition, a user-defined FORTRAN subroutine VUMAT suitable for the ABAQUS/Explicit solver and an analysis algorithm were established to obtain a progressive damage prediction of the CFRP layer using the three-dimensional Hashin failure criterion. Furthermore, the failure mechanism of the two types of CARALL beams was numerically analyzed in detail.

2 Experimental procedures

2.1 Specimen preparation

In decomposable truss bridges, the beam members are typically designed as double-channel cross-sectional profiles to improve the overall and local stabilities of the channel beams. Herein, the double-channel cross-sectional beam is composed of two single-channel cross-sectional components, as illustrated in Figure 1. The entire preparation procedure for the CARALL double-channel specimen is as follows. First, the CARALL single-channel components were fabricated via the pressure molding thermal curing forming process. Second, Q235 steel blocks were set between the webs at the ends of the two single-channel members as the connecting pieces. The connecting steel blocks and the single-channel members' webs were bonded with Loctite 9514 super glue. The Y-direction height of the connecting piece was 40 mm, X-direction thickness was 10 mm,

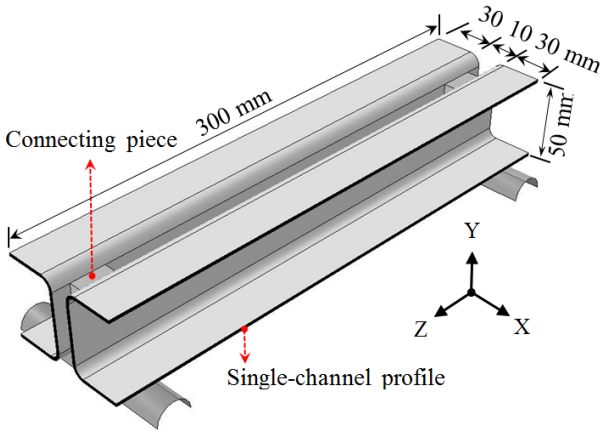

Figure 1: Configuration of CARALL beam with a double-channel cross-section.

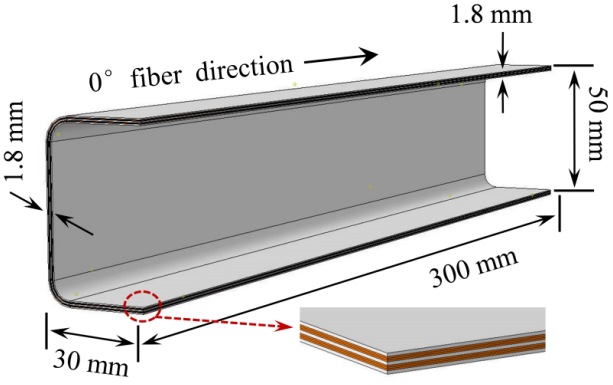

Figure 2: Configuration of CARALL beam with a single-channel cross-section.

Table 1: Double-channel cross-section member notations, layup sequence, and dimensions (unit: mm).

Specimen	Layup configuration	Al	Thickness	Length	Width	Height
SHCXL-A	$Al/[0/90/0]_3/Al/[0/90/0]_3/Al$	2024-T3	1.8	300	30	50
SHCXL-B	$Al/[45/0/-45]_3/Al/[-45/0/45]_3/Al$	2024-T3	1.8	300	30	50

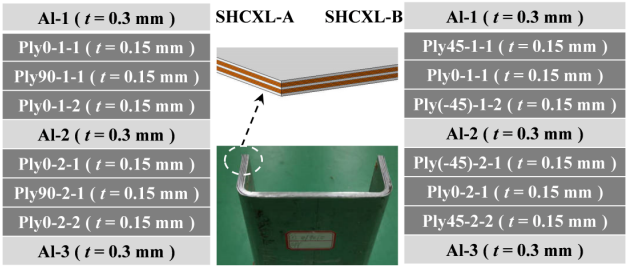

Figure 3: Stack and fiber ply configurations of CARALL specimens.

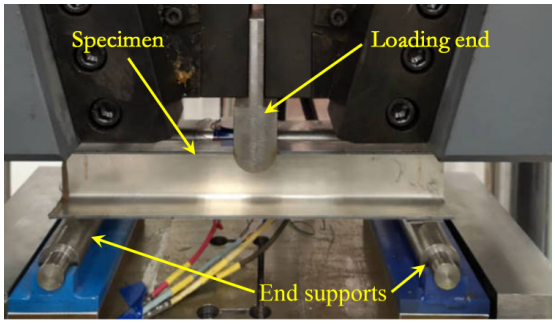

Figure 4: Three-point bending test setup for double-channel CARALL beam.

and Z-direction length was 20 mm. For the CARALL single-channel components, the overall dimensions were 300 mm, 30 mm, and 50 mm in length, width, and height, respectively. The wall thickness was 1.8 mm. The laminated configuration was composed of three layers of aluminum alloy sheets and two layers of CFRP laminated sheets, as depicted in Figure 2. Herein, the longitudinal direction of the channel-shaped beam was defined as the 0° direction of the fiber.

The specific laminate and fiber layup configurations of the specimen are depicted in Figure 3. In the experiments, two different fiber layup configurations, referred to as Al/0°/90°/0°/Al/0°/90°/0°/Al and Al/45°/0°/−45°/Al/−45°/0°/45°/Al, were employed in the fabrication of the single-channel components. In this case, two sets of specimens with different fiber layup configurations were prepared and marked as SHCXL-A and SHCXL-B, respectively. Three specimens were prepared for each set of specimens. The SHCXL-A group numbers were SHCXL-A-1, SHCXL-A-2, and SHCXL-A-3; the SHCXL-B group numbers were SHCXL-B-1, SHCXL-B-2, and SHCXL-B-3. The CFRP layers used in the study were T700/E-302 carbon fiber epoxy prepregs (unidirectional board) with a thickness of 0.15 mm provided by Sichuan Xinwanxing Composite Material Co., Ltd. The selected aluminum alloy was 2024-T3 with a thickness of 0.3 mm.

2.2 Three-point bending test

As there exists no unified standard for the bending loading test of CARALL double-channel cross-sectional members, a self-designed three-point bending test method was adopted in this study, as depicted in Figure 4. The double-channel cross-sectional specimen was set as a simplified supporting condition, and two rolling bars were used as end supports. The center points between the two rolling supports were 260 mm long. A concentrated load F was directly applied on the upper surface of the beam members at mid-span. The loading process was completed using a WANCE microcomputer controlled by an electro-hydraulic servo universal testing machine (1000 kN) from the Shenzhen Wance Test Equipment Co., Ltd. Displacement loading was adopted, and the loading rate was set to 1 mm/min. Considering the research purpose, only the ultimate bearing capacity and failure modes of the specimens were determined in the test.

3 Experimental results

The failure modes and ultimate bearing capacity of the SHCXL-A and SHCXL-B beams with double-channel cross-sections are summarized in Table 2. The real damage and failure modes after the specimens lose their bearing capacity are depicted in Figure 5. Only a few differences were observed in the ultimate bearing capacity and the overall failure mode between the two types of specimens with different carbon fiber layers. The ultimate loads acting on the mid-span position of the SHCXL-A and SHCXL-B beams varied from 5.3 to 6.0 kN. The final failure mode under a three-point bending load was as follows. At the concentrated loading position, the connection location of the up-

Table 2: Bearing capacity and failure modes of double-channel CARALL beams with different fiber layups.

Specimen	Layup configuration	Failure modes	Ultimate load (kN)
SHCXL-A-1	0°/90°/0°	At the mid-span position, the connection location of the upper flanges and webs produced a large buckling deformation. The connecting pieces between the members with a single-channel cross-section fell off. The upper flange was locally bent and deformed, and interlayer delamination damage failure between the material layers of the upper flange occurred.	5.496
SHCXL-A-2	0°/90°/0°		5.965
SHCXL-A-3	0°/90°/0°		5.768
SHCXL-B-1	45°/0°/−45°	At the mid-span position, the connection location of the upper flanges and webs produced a large buckling deformation. The connecting pieces between the members with a single-channel cross-section fell off. The upper flange was locally bent and deformed, and interlayer delamination damage failure between the material layers of the upper flange occurred.	5.386
SHCXL-B-2	45°/0°/−45°		5.894
SHCXL-B-3	45°/0°/−45°		5.645

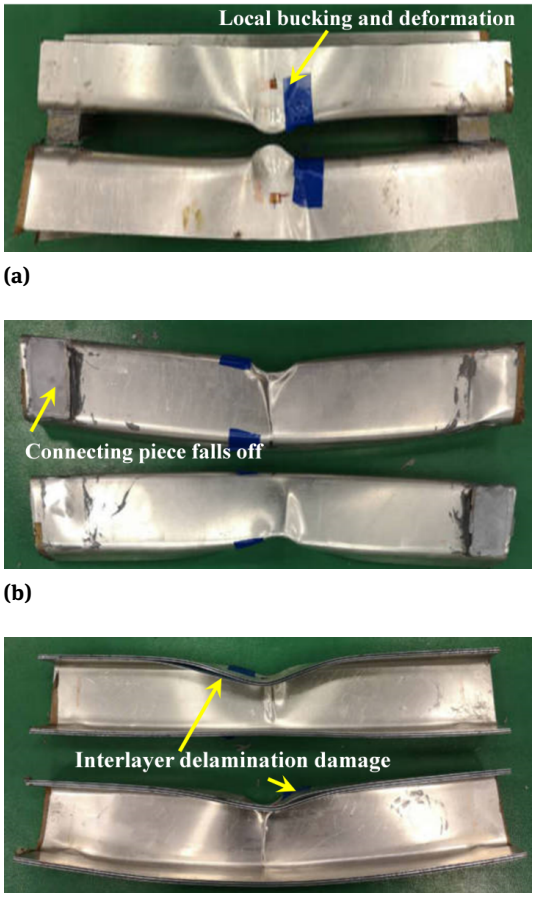

Figure 5: Failure modes of double-channel CARALL beams: (a) Local buckling and deformation of the upper flange and web; (b) connecting pieces fall off; and (c) interlayer delamination damage of upper flange.

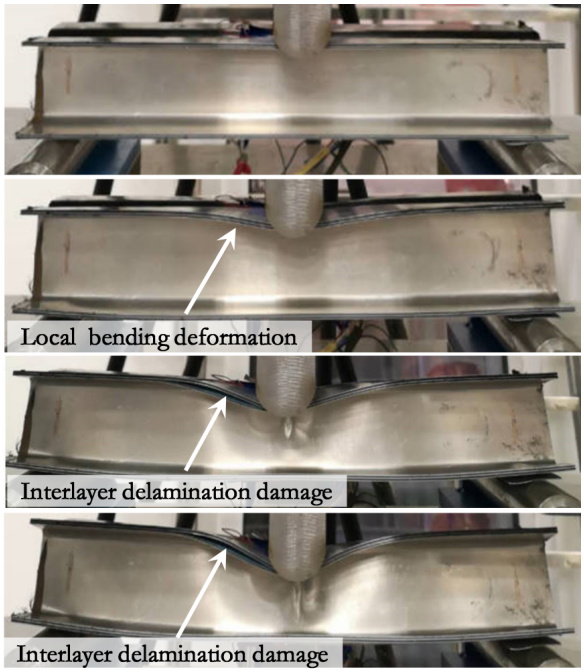

Figure 6: Deformation and failure evolution process of double-channel CARALL beams.

per flanges and webs first produced large buckling deformations. Subsequently, the two connecting pieces between the members with a single-channel cross-section fell off. Finally, owing to the large local bending deformation of the upper flange at the concentrated loading position, significant interlayer delamination damage occurred between the material layers of the upper flange, and finally, failure of the beam components occurred.

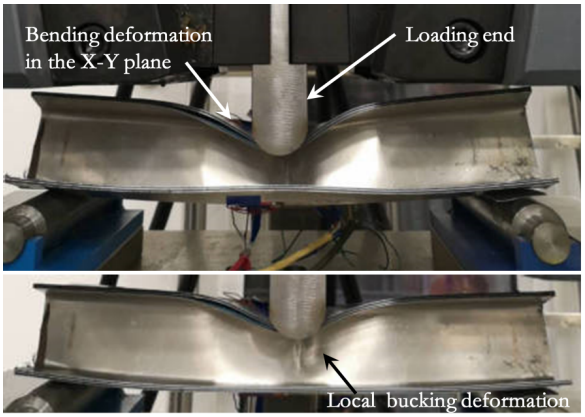

Figure 7: Local bending deformation in X-Y plane of double-channel CARALL beams.

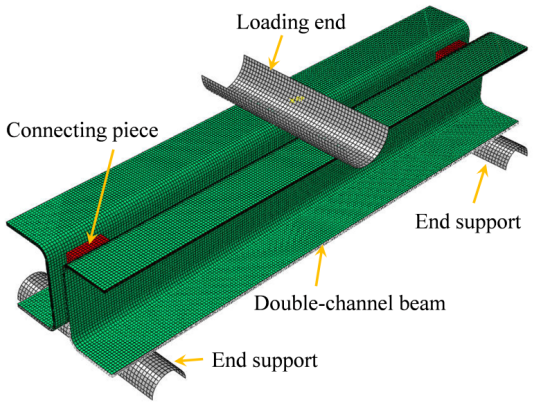

Figure 8: Finite element model of double-channel CARALL beams subjected to three-point bending loads.

Figure 6 illustrates the deformation and failure evolution process of the double-channel CARALL beams. From Figure 5(a) and Figure 6, it can be seen that the ultimate bending bearing capacities of the SHCXL-A and SHCXL-B beams were dependent on the beams' abilities to resist buckling deformation of the CARALL at the connection between the upper flanges and webs. The upper flange of the double-channel beams exhibited a high bending resistance in the X-Y plane, and the bending bearing capacity of the beam components was high. This is because the upper flange at the concentrated loading position can be regarded as a cantilever beam, if the location of the connection between the flange and web is considered as the fixed end. The loading end was equivalent to applying a distributed load to the upper flange. The upper flange then produced a large local bending deformation in the X-Y plane (see Figure 7), which caused a large local bending deformation of the connection between the upper flange and web. With an increase in the bending deformation, interlayer delamination failure of the laminate finally occurred (see Figures 6 and 7).

Thus, it can be concluded that, because the upper flange of the double-channel CARALL beam member exhibited poor resistance to the bending deformation in the X-Y plane, the beam members produced a large local bending deformation at the concentrated loading position. The large local bending deformation finally caused the beam to lose its bearing capacity. The resistance to local bending deformation at the junction of the flange and web determined the ultimate load-bearing capacity of the beam, which resulted in small differences between the ultimate bearing capacity of the two types of beams with different fiber layup configurations ($0°/90°/0°$ and $45°/0°/-45°$).

4 Numerical analysis

4.1 Finite element modeling

With the aid of the ABAQUS software, the explicit time integration method (ABAQUS/Explicit) was used to simulate the bending bearing performance and failure mechanism of the aforementioned two types of double-channel CARALL beams. Owing to the limitation of the two-dimensional Hashin failure criterion in ABAQUS, a VUMAT subroutine suitable for the ABAQUS/Explicit solver was developed in FORTRAN to realize the CFRP layer progressive damage simulation based on the three-dimensional Hashin failure criterion.

Figure 8 depicts the established finite element (FE) model of the double-channel CARALL beams subjected to three-point bending loads. The three-dimensional progressive damage model was used as the material model of the CFRP layers, and the eight-node reduced integral solid element (C3D8R) was used for the element model of the CFRP layers. The elastoplastic constitutive and Johnson-Cook plastic damage criterion [17] were used for the aluminum alloy material, and the aluminum alloy layer was also discretized by the C3D8R element.

Note that a key technique in the FE analysis is to simulate delamination growth in composite laminates. Different cohesive models have been used in some existing literatures [43–46]. In this paper, the delamination failure prediction between the layers in the laminated beam was simulated by the cohesive zone model (CZM) method, and was realized by the established three-dimensional cohesive unit COH3D8. The used CZM method to simulate interfacial failure is achieved by defining the surface-based cohesive contact. It allows the specification of generalized traction-

separation behavior of two adjacent surfaces without the need to employ the cohesive element. The detail cohesive algorithm selected to handle such interfacial problems can be found in a previous work [17].

To finely simulate the influence of the concentrated load F and to meet the requirements of the element characteristic length while improving the calculation efficiency, the element grid size was set as 1.5 mm × 1.5 mm. The loading end was coupled to all the nodes through the reference point at mid-span, and a displacement of 25 mm along the height direction was applied to the reference point.

4.2 Simulation analysis results

Figure 9 depicts the final failure modes of the two types of double-channel CARALL beams under three-point bending loads. According to the numerical simulation results, the maximum concentrated loads of the two types of beams with different fiber layers were 7.078 kN and 6.824 kN for SHCXL-A and SHCXL-B, respectively. By comparing Figure 5 and Figure 9, it can be observed that, in terms of the final failure modes of the CARALL beams, the numerical simulation are consistent with the experimental results, both of which demonstrate that a large local bending deformation and delamination failure occur at the junction of the upper flange and web of the channel beam.

However, with regard to the ultimate bearing capacity of the beams, there is a difference between the numerical simulation and experimental results. The ultimate load obtained by the numerical simulation was greater than the experimental result, as presented in Table 3. The main reason for the relatively large error is that the numerical simulation results were obtained under ideal conditions. For example, ideal bonding conditions between the layers of the laminate were assumed in the simulation. However, during the pressure molding thermal curing forming process of the specimens, the operating errors of the personnel and the machining quality were likely to affect the load-

Table 3: Comparison of ultimate bearing capacities obtained in numerical simulation and experiment.

Specimen	Layup configurations	Ultimate loads (kN)		Error
		Simulation	Experiment	
SHCXL-A-1	0°/90°/0°	7.078	5.496	28.7%
SHCXL-A-2	0°/90°/0°	7.078	5.965	18.7%
SHCXL-A-3	0°/90°/0°	7.078	5.768	22.7%
SHCXL-B-1	45°/0°/−45°	6.823	5.386	26.7%
SHCXL-B-2	45°/0°/−45°	6.823	5.894	15.8%
SHCXL-B-3	45°/0°/−45°	6.823	5.645	21.0%

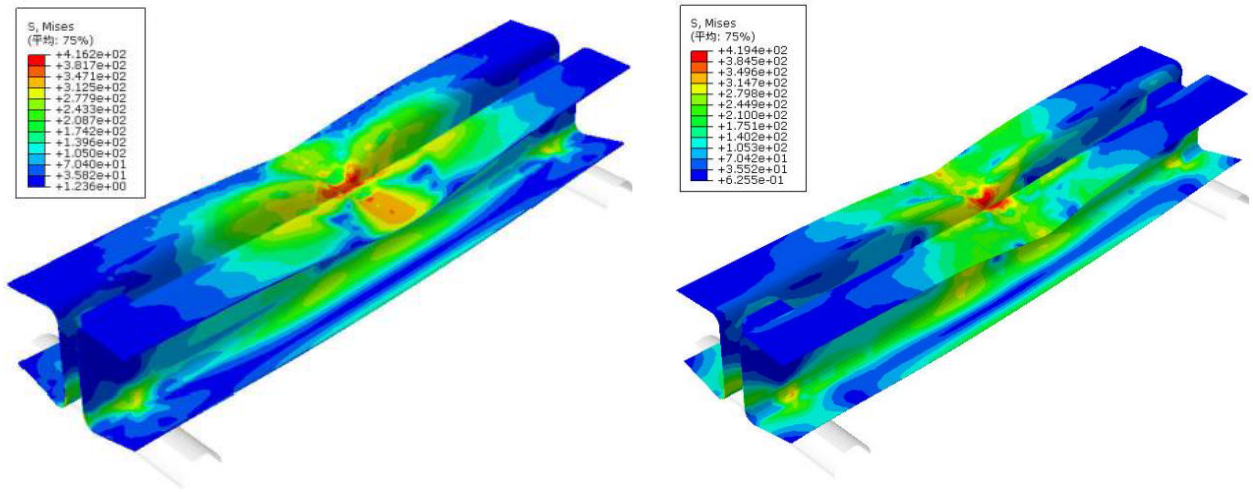

(a) (b)

Figure 9: Numerical results of failure modes of double-channel CARALL beams: (a) SHCXL-A and (b) SHCXL-B.

bearing capacity of the fabricated beams. In general, under ideal conditions, the error can be controlled within 30%.

4.3 Failure mechanism analysis

4.3.1 Failure analysis of aluminum alloy sheet

According to the comparative analysis, the outer aluminum alloy sheet of the beam was the first to produce buckling deformation, and the damage was the most severe when the beam lost its bearing capacity. Therefore, the failure mechanism of the double-channel beam under a concentrated load at mid-span was analyzed according to the stress and deformation process of the outer aluminum alloy sheet, as depicted in Figure 10. For the SHCXL-A and SHCXL-B beams, when the mid-span concentrated load only reached 1.035 kN and 1.519 kN respectively, the maximum stress of the outer aluminum alloy sheet reached 309.6 MPa and 319.4 MPa at the junction of the upper flange and web respectively. When the plastic strain of the 2024-T3 aluminum alloy was zero, the yield stress was only 300 MPa. This implies that the outer aluminum alloy sheet had already undergone local plastic deformation at this time. This is mainly attributed to the fact that the upper flange at the concentrated loading position is equivalent to a cantilever beam. The distributed load due to the loading end caused the upper flange to produce a large local bending deformation in the X-Y plane (see Figure 7), thereby resulting in a large local buckling deformation of the outer aluminum alloy sheet at the junction of the upper flange and the web of the beam.

When the concentrated load at the mid-span reached 3.660 kN and 3.066 kN respectively (see Figure 10), the upper flange at the concentrated load location of the SHCXL-A and SHCXL-B beams exhibited more obvious local buckling deformation, making the stress levels of the outer aluminum alloy sheets at the junction of the upper flange and the web 351.4 MPa and 330.8 MPa, respectively. This indi-

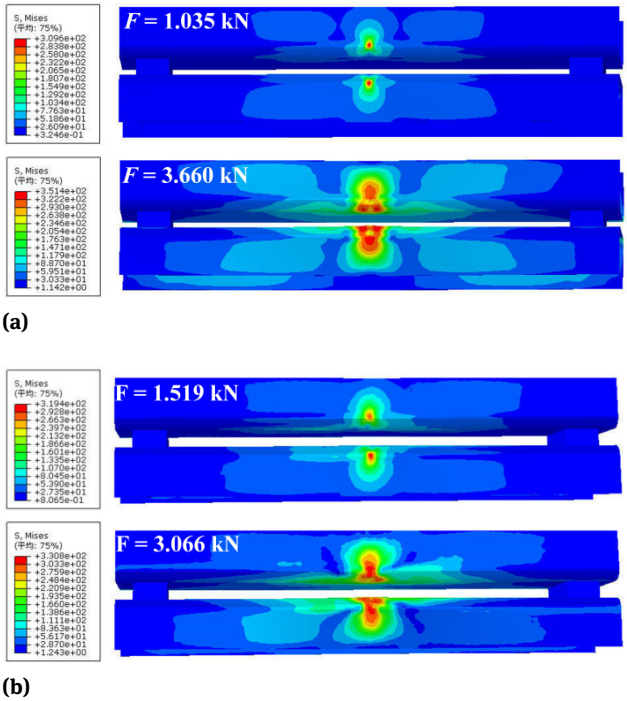

Figure 10: Stress distribution and deformation of outer aluminum sheet under different concentrated loads: (a) SHCXL-A and (b) SHCXL-B.

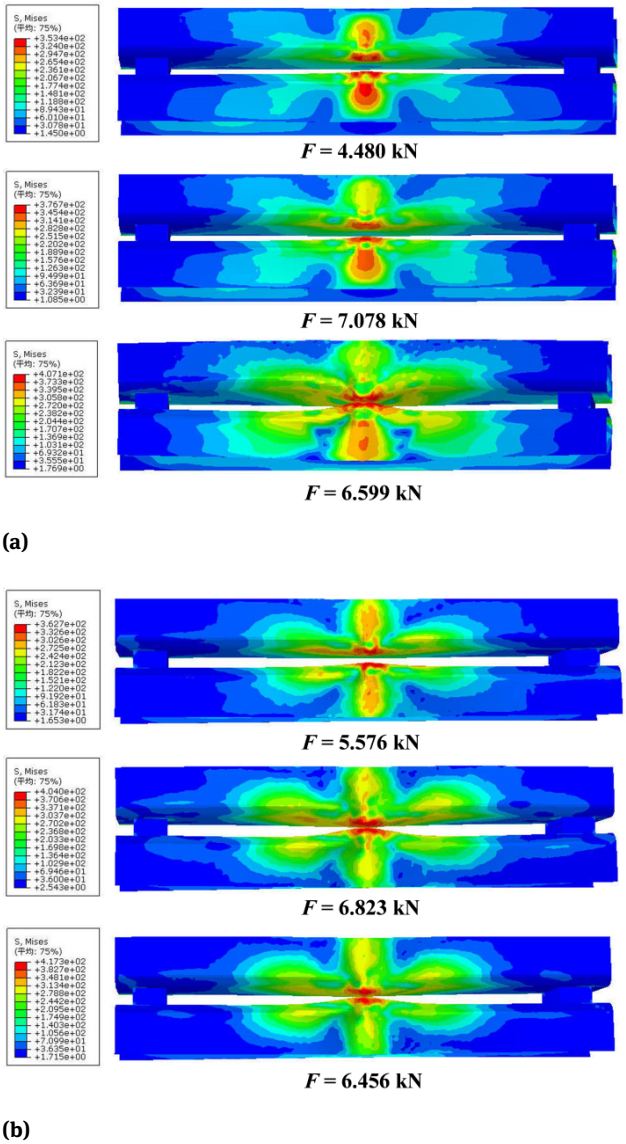

Figure 11: Stress and deformation evolution in outer aluminum sheet of double-channel CARALL beams: (a) SHCXL-A and (b) SHCXL-B.

cates that the bending deformation in the X-Y plane of the upper flange increased, resulting in a larger plastic deformation of the outer aluminum alloy sheet at the junction of the flange and web. However, at this time, the distribution range of the high-stress area was still relatively small, and the beam webs did not exhibit any evident local bending deformation. The above phenomenon also indicates that the upper flange of the beam with a fiber layer of 45°/0°/−45° had a strong ability to resist bending deformation (concentrated load: 1.519 kN > 1.035 kN). Once the aluminum alloy sheet deformed plastically, its ability to resist bending deformation in the X-Y plane reduced (concentrated load: 3.066 kN < 3.660 kN).

When the concentrated loads acting on the SHCXL-A and SHCXL-B beams reached 4.480 kN and 5.576 kN respectively (see Figure 11), the local buckling deformation of the outer aluminum alloy sheet at the connection between the upper flanges and webs was relatively obvious. Moreover, the high-stress distribution area also increased. When the concentrated loads acting at the mid-span reached the ultimate bearing capacities of 7.078 kN and 6.823 kN, the stresses acting on the outer aluminum alloy sheet were 376.7 MPa and 404 MPa, respectively, and more obvious local buckling deformation occurred at the junction of the upper flange and web. At this time, the concentrated load acting on the SHCXL-A beam was larger than that acting on the SHCXL-B beam (7.078 kN > 6.823 kN). However, the stress acting on the outer aluminum alloy sheet decreased (376.7 MPa < 404 MPa), which further indicated that once the aluminum alloy sheet deformed plastically, the upper flange of the CARALL beam with the fiber layup configuration of 0°/90°/0° had a strong ability to resist bending deformation in the X-Y plane.

In conclusion, the above results further verify that the key factors leading to the loss of the ultimate bearing capacity of the beam members are that the upper flange of the double-channel CARALL beam is equivalent to a cantilever beam with elastic restraint fixed ends under a distributed load, and that the junction of the upper flange and web continuously provides the bending load in the X-Y plane to the web, resulting in a larger local buckling deformation.

4.3.2 Failure analysis of interlaminar delamination

According to the comparative analysis, there were large interlaminar delamination failure areas between the fiber layer of ply0-1-1 (or the fiber layer of ply45-1-1) and its adjacent layers, and between the ply90-1-1 fibre layer and its adjacent layers. The degree of damage was the most severe when the CARALL beam collapsed. Therefore, the evolution

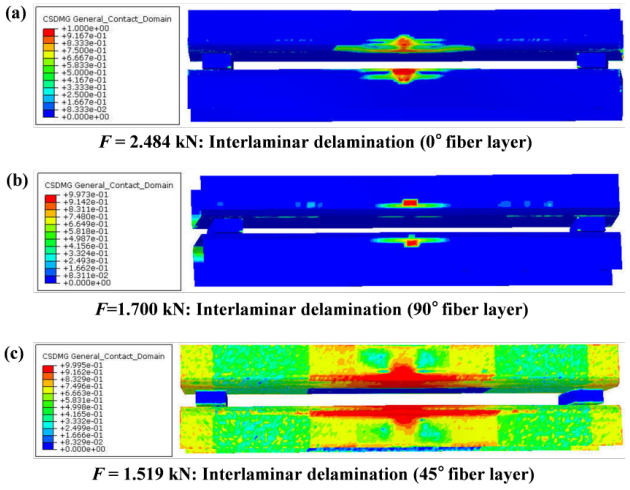

Figure 12: Initial interlaminar delamination failure area distribution of double-channel CARALL beams: (a) SHCXL-A: 0° fiber layer; (b) SHCXL-A: 90° fiber layer; and (c) SHCXL-B: 45° fiber layer.

of the interlaminar delamination failure for each layer of the laminated panels was analyzed on the basis of the interlaminar delamination between the fiber layer of ply0-1-1 or the fiber layer of ply45-1-1 and its adjacent layers, and between the ply90-1-1 fiber layer and its adjacent layers. The first 0° CFRP fiber layer in the 3/2 laminated panels of SHCXL-A was designated as ply0-1-1. The first 45° CFRP fiber layer of SHCXL-B was designated as ply45-1-1. The first 90° fiber layer was designated as ply90-1-1, as depicted in Figure 3.

As illustrated in Figures 12a and 12b, when the concentrated load on the SHCXL-A beam reached approximately 2.484 kN and 1.7 kN, the stratification evolution factors began to appear between the fiber layer of ply0-1-1 and its adjacent layers and between the fiber layer of ply90-1-1 and its adjacent layers, respectively. When the concentrated load on the SHCXL-B beam reached approximately 1.519 kN, interlaminar delamination began to appear between the ply45-1-1 fiber layer and its adjacent layers (see Figure 12c). Moreover, the extension area of the interlayer delamination failure was large. This indicates that, in the initial state of the concentrated load bearing of the beam, the resistance of the 0° fiber layer to delamination was stronger than that of the 90° and 45° fiber layers. This implies that the fiber orientation angle weakens the ability of the fiber layer to resist interlaminar delamination damage.

For the SHCXL-A and SHCXL-B beams, when the concentrated loads reached the ultimate bearing capacities of the two types of beams, the delamination failure area evidently increased in comparison with that of the previously mentioned results (see Figure 13). The failure area of the interlaminar delamination between the ply45-1-1 fiber

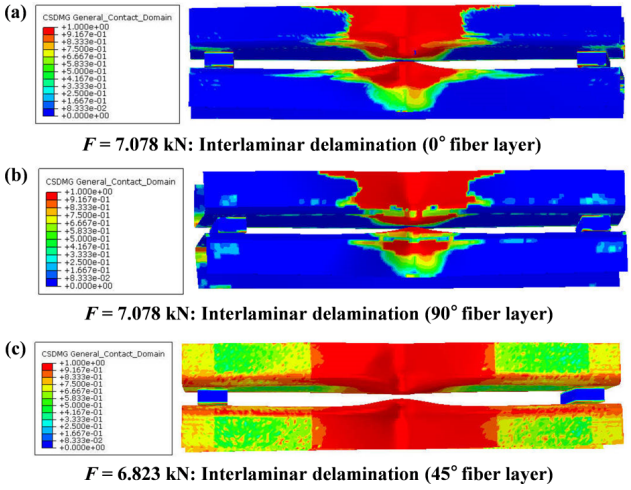

Figure 13: Delamination failure area distribution of double-channel CARALL beams in ultimate bearing state: (a) SHCXL-A: 0° fiber layer; (b) SHCXL-A: 90° fiber layer; and (c) SHCXL-B: 45° fiber layer.

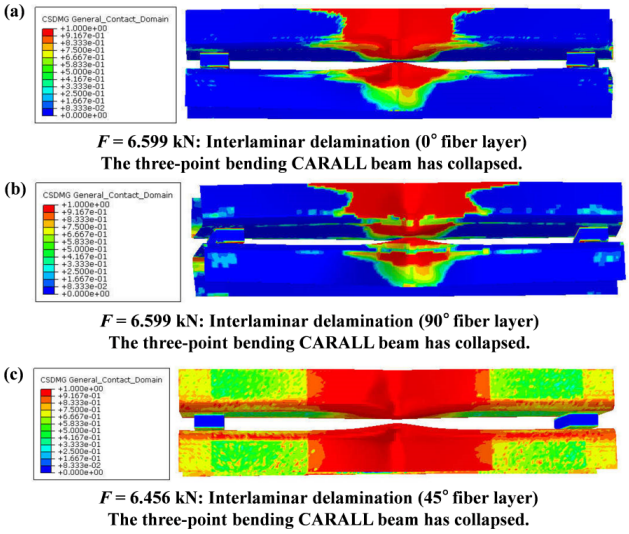

Figure 14: Delamination failure area distribution of double-channel CARALL beams at final failure state: (a) SHCXL-A: 0° fiber layer; (b) SHCXL-A: 90° fiber layer; and (c) SHCXL-B: 45° fiber layer.

layer and the adjacent layers of the SHCXL-B beam was the largest (see Figure 13c), and the delamination failure area between the ply90-1-1 fiber layer and its adjacent layers was the smallest (see Figure 13b). Delamination failure between the 0° or 90° fiber layer and its adjacent layers mainly occurred at the flange and at the junction of the web and flange of the double-channel beams. Interlaminar delamination failure occurred between the 45° fiber layer and the adjacent layers on the web and flange within a large area (see Figure 13c).

With regard to the SHCXL-A and SHCXL-B beams (see Figure 14), the failure degree and failure area of the delamination between the ply0-1-1 or ply90-1-1 and ply45-1-1 fiber layers and their adjacent layers on the flange were greater than those in the previously mentioned results (see Figures 12 and 13). In comparison with the delamination failure between the 90° (or 0°) fiber layer and the adjacent fiber layer of the SHCXL-A beam, the failure area and failure degree between the 45° fiber layer and the adjacent fiber layer of the SHCXL-B beam were larger. Moreover, the connection between the flanges and webs was completely stratified along the length of the double-channel beam.

With a gradual increase in the concentrated load, the delamination failure area between the ply0-1-1, ply90-1-1, and ply45-1-1 fiber layers, and their adjacent layers gradually expanded. The delamination failure area was still local until the beam lost its bearing capacity. In the longitudinal direction, a larger range of delamination failure occurred only near the concentrated loading position at the mid-span of the CARALL beams. These local interlayer delamination failures caused separation between the laminated layers and reduced the ability of the upper flange to resist bending deformation. Therefore, the interlayer delamination failure was the main factor for the loss of the bearing capacity of the CARALL beams. In addition, regardless of the load level, the delamination failure distribution area between the ply0-1-1 (or ply90-1-1) fiber layer and its adjacent layers for the SHCXL-A beam was smaller than that of the ply45-1-1 fiber layer and its adjacent layers for the SHCXL-B beam, which suggests that, in comparison with the 0° or 90° fiber layup, the 45° fiber layup had a weaker ability to resist delamination damage between layers.

4.3.3 Failure analysis of fiber tension and compression

Figures 15 and 16 depicts the damage evolution process of the fiber tensile and compression failures for the ply0-1-1, ply90-1-1, and ply45-1-1 fiber layers in the CFRP prepregs of the two types of beams with different fiber layups. When the two types of beams lost their bearing capacity and collapsed, the fiber tensile damage was almost zero, and the fiber compression damage was only slightly more severe than the tensile damage. A layer-by-layer analysis reveals that the fiber tensile and compression damage levels of all other fiber layers were smaller than those of ply0-1-1 or ply90-1-1 and ply45-1-1 fiber layers. It can be concluded that, when the main damage mode and the corresponding deformation of the double-channel CARALL beams were the local bending and buckling deformation of the flange and web, the fiber tensile and compression damage had almost no effect on the overall failure of the beams.

4.3.4 Failure analysis of matrix tension and compression

Figures 17 to 22 illustrate the evolution of the tensile and compression damage on the fiber layer matrix of ply0-1-1, ply90-1-1, and ply45-1-1 in CFRP prepregs of the two different types of double-channel CARALL beams subjected to three-point bending loads. When the mid-span acting concentrated loads of the two types of double-channel CARALL beams reached 0.486 kN, 3.659 kN, and 1.519 kN, the matrix of ply0-1-1, ply90-1-1, and ply45-1-1 fiber layers had already suffered tensile and compression damage. Therefore, assuming that the main failure modes of the double-channel CARALL beam members were the local buckling deformation of the flange and web under concentrated loads, the ability to resist matrix tension and compression damage for the fiber layers decreased in the order 90° fiber layer > 45° fiber layer > 0° fiber layer at the initial stage of load bearing.

When the load acting at the mid-span of the laminated beam reached the ultimate bearing capacity and the laminated beam lost its bearing capacity, the matrix tensile

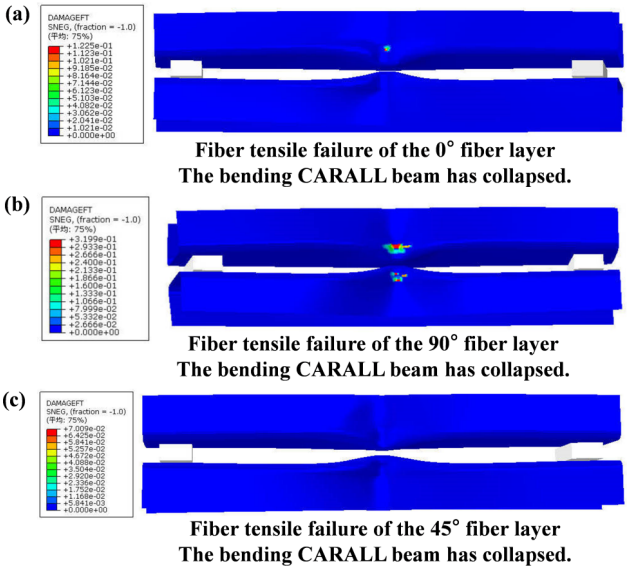

Figure 15: Failure evolution process of fiber tension in CFRP layers of double-channel CARALL beam: (a) SHCXL-A: 0° fiber layer; (b) SHCXL-A: 90° fiber layer; and (c) SHCXL-B: 45° fiber layer.

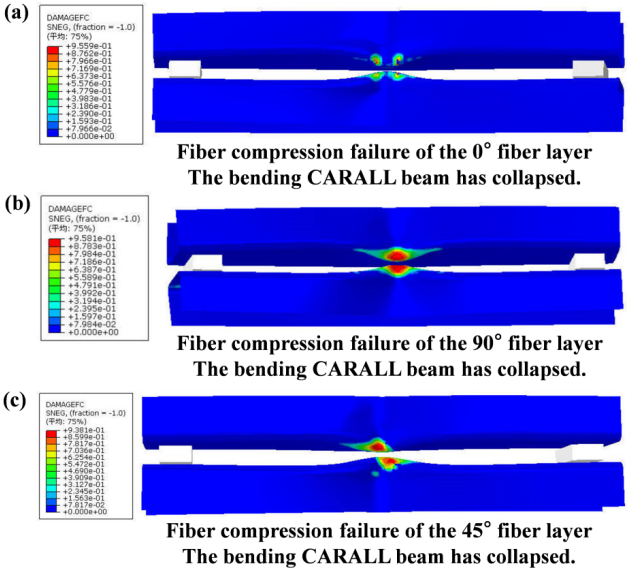

Figure 16: Failure evolution process of fiber compression in CFRP layers of double-channel CARALL beam: (a) SHCXL-A: 0° fiber layer; (b) SHCXL-A: 90° fiber layer; and (c) SHCXL-B: 45° fiber layer.

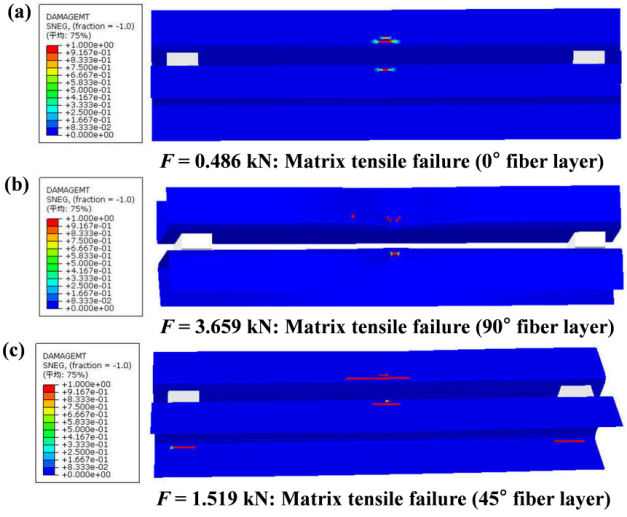

Figure 17: Initial matrix tensile failure area distribution of fiber layers of double-channel CARALL beam: (a) SHCXL-A: 0° fiber layer; (b) SHCXL-A: 90° fiber layer; and (c) SHCXL-B: 45° fiber layer.

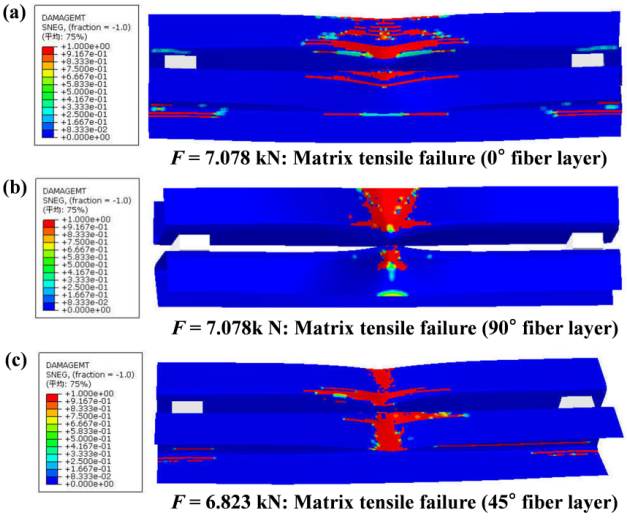

Figure 18: Matrix tensile failure area distribution of fiber layers in ultimate bearing state: (a) SHCXL-A: 0° fiber layer; (b) SHCXL-A: 90° fiber layer; and (c) SHCXL-B: 45° fiber layer.

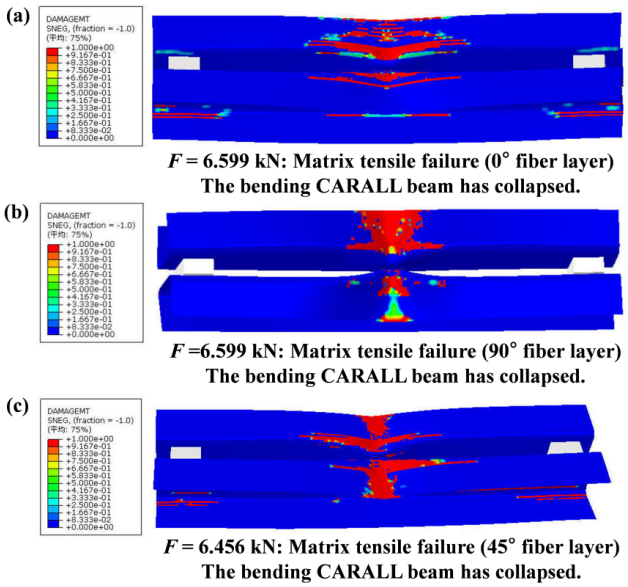

Figure 19: Matrix tensile failure area distribution of fiber layers in final failure state: (a) SHCXL-A: 0° fiber layer; (b) SHCXL-A: 90° fiber layer; and (c) SHCXL-B: 45° fiber layer.

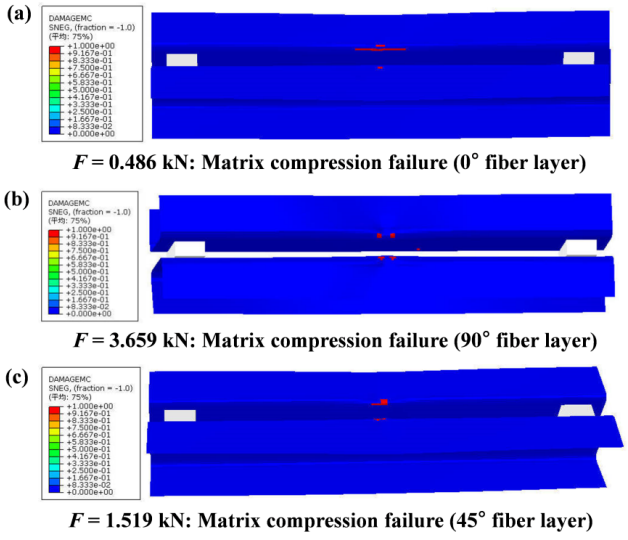

Figure 20: Initial matrix compression failure area distribution of fiber layers: (a) SHCXL-A: 0° fiber layer; (b) SHCXL-A: 90° fiber layer; and (c) SHCXL-B: 45° fiber layer.

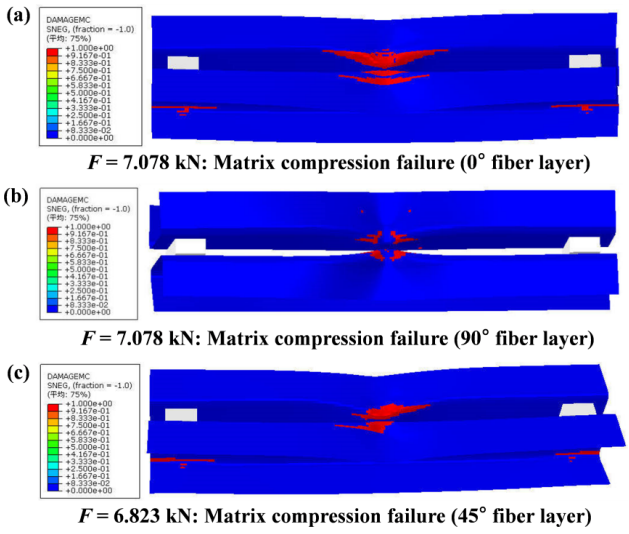

Figure 21: Matrix compression failure area distribution of fiber layers in ultimate bearing state: (a) SHCXL-A: 0° fiber layer; (b) SHCXL-A: 90° fiber layer; and (c) SHCXL-B: 45° fiber layer.

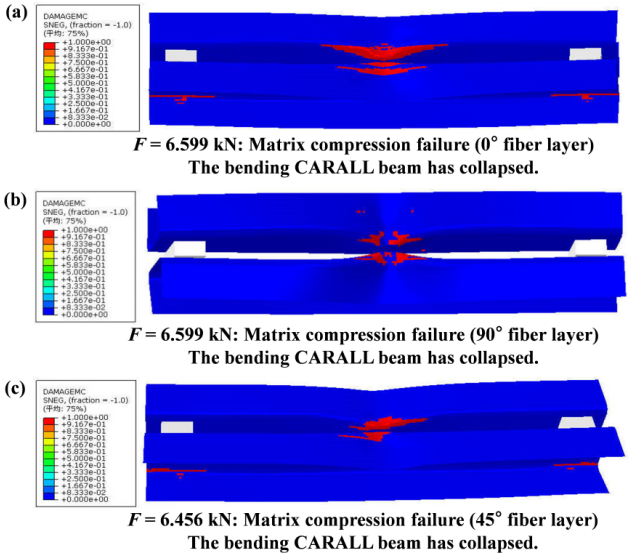

Figure 22: Matrix compression failure area distribution of fiber layers in final failure state. (a) SHCXL-A: 0° fiber layer; (b) SHCXL-A: 90° fiber layer; and (c) SHCXL-B: 45° fiber layer.

failure areas of the ply0-1-1 fiber layer were distributed in stripes, while the matrix tensile failure areas of the ply90-1-1 and ply45-1-1 fiber layers were distributed in blocks (see Figures 18 and 19). This implies that under the existing loading conditions, the ply0-1-1 fiber layer exhibits the strongest ability to resist matrix tensile damage.

As can be seen from Figures 21 and 22, the matrix compression failure distribution areas of the ply0-1-1, ply90-1-1, and ply45-1-1 fiber layers assumed a block-like distribution, and size of the distribution areas was arranged in the order of 90°, 45°, and 0°. Thus, it can be concluded that their ability to resist matrix compression damage decreased in the order 90° fiber layer > 45° fiber layer > 0° fiber layer.

4.3.5 Shear failure analysis of fiber layer

Figures 23 to 25 depict the shear failure evolution process of ply0-1-1, ply90-1-1, and ply45-1-1 fiber layers in CFRP prepregs of the two different types of beams under three-point bending loads. When the double-channel CARALL beams with

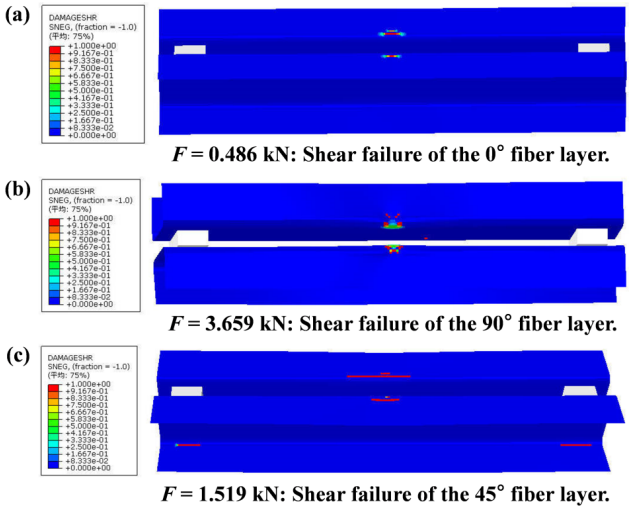

Figure 23: Initial shear failure area distribution of fiber layers: (a) SHCXL-A: 0° fiber layer; (b) SHCXL-A: 90° fiber layer; and (c) SHCXL-B: 45° fiber layer.

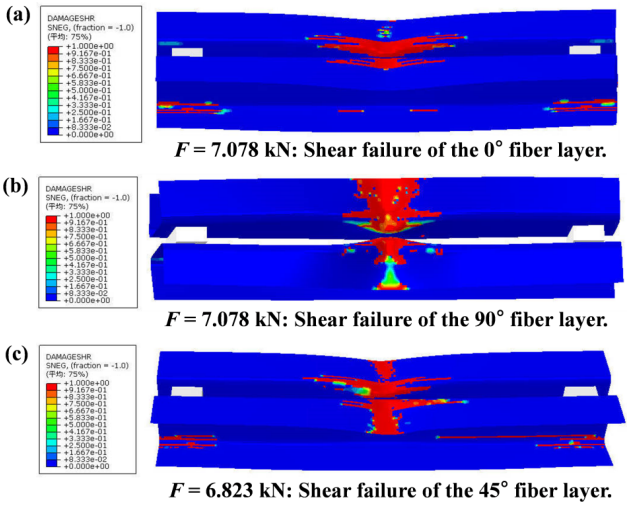

Figure 24: Shear failure area distribution of fiber layers in ultimate bearing state: (a) SHCXL-A: 0° fiber layer; (b) SHCXL-A: 90° fiber layer; and (c) SHCXL-B: 45° fiber layer.

the 0°/90°/0° fiber layups were subjected to a concentrated load of 0.486 kN at the mid-span (see Figure 23a), the shear damage failure of the ply0-1-1 fiber layer had already occurred. However, the concentrated load of the double-channel beams with 45°/ 0°/−45° fiber layups must reach 1.519 kN for shear damage failure of the ply45-1-1 fiber layer to occur (see Figure 23c). For the double-channel CARALL beam members with the 0°/90°/0° fiber layups, the shear failure of the ply90-1-1 fiber layer occurred only when the concentrated load reached 3.659 kN (see Figure 23b). This indicates that, at the initial stage of load bearing, the ability of the ply90-1-1 fiber layer to resist the shear damage failure of the double-channel beams was stronger than that of the ply0-1-1 and ply45-1-1 fiber layers.

In addition, after the double-channel CARALL beam reached its ultimate bearing capacity and lost its load-bearing ability, the shear failure distribution areas of the fiber layer of ply0-1-1 and ply45-1-1 were in strips and blocks. However, the shear failure distribution areas of the fiber layer of ply90-1-1 were in blocks (see Figures 24 and 25). The shear damage failure distribution area of the ply0-1-1 fiber layer was smaller than those of the ply45-1-1 and ply90-1-1 fiber layers, which further indicated that, in comparison with the ply90-1-1 and ply45-1-1 fiber layers, the ply0-1-1 fiber layer exhibited stronger resistance to shear failure. As the load continued to increase, the shear failure range of the ply0-1-1, ply90-1-1, and ply45-1-1 fiber layers gradually expanded, which undoubtedly intensified the local bending deformation at the junction of the flange and web of the double-channel CARALL beams, causing the beams to lose their overall bearing capacity.

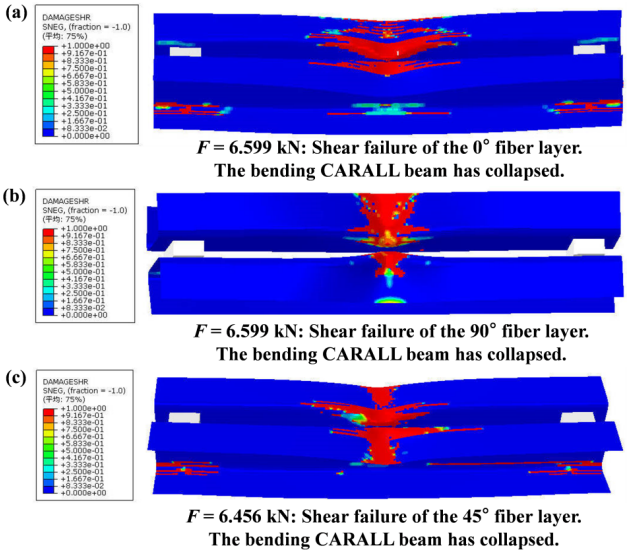

Figure 25: Shear failure area distribution of fiber layers in final failure state: (a) SHCXL-A: 0° fiber layer; (b) SHCXL-A: 90° fiber layer; and (c) SHCXL-B: 45° fiber layer.

5 Conclusions

In this study, two sets of double-channel CARALL beams using different fiber layup configurations ($[0°/90°/0°]_3$ and $[45°/0°/-45°]_3$) were prepared via the pressure molding thermal curing forming process and subjected to three-point bending loads. The flexural bearing capacity and failure mechanism of the CARALL beams were experimentally and numerically studied. The major findings of this study can be summarized as follows:

(1) Owing to the weak bending resistance of the laminated beam flange in the X-Y plane, the final failure mode of the two types of CARALL beams under the concentrated load at mid-span was the local large bending deformation at the junction of the flange and web. This failure mode indicated that different fiber layup configurations had no evident influence on the bending bearing performance of the double-channel CARALL beam. The ultimate bending bearing capacity of both types of beams was not high, and the materials were not fully utilized.
(2) The ultimate loss of load-bearing capacity of the two types of CARALL beams was caused by the large local bending and buckling damage generated at the junction of the upper flange and web rather than by the damage of the aluminum sheet or the fiber tensile or compression failure of the CFRP prepregs. The large local bending and buckling damage was mainly caused by the interlaminar delamination damage between each unidirectional laminated plate at the concentrated loading position, matrix tensile or compression damage, and shear failure of the fiber layers.
(3) At the initial stage of damage, the resistance of the fiber layers of the laminated beams to fiber tensile and compression damage, matrix tension and compression damage, and shear damage of fiber layers decreased in the order 90° fiber layer > 45°fiber layer > 0° fiber layer. The resistance of the fiber layers to interlaminar delamination damage decreased in the order 0° fiber layer > 90° fiber layer > 45° fiber layer. Therefore, it is suggested that the load-bearing performance could be improved if the three laminated fiber layers, *i.e.*, the 90°, 0°, and 45° fibers, are mixed.
(4) The VUMAT subroutine based on FORTRAN for the ABAQUS/Explicit display analysis algorithm can be used to reveal the progressive damage of the CFRP layer with the three-dimensional Hashin progressive damage criterion. When factors, such as specimen preparation and test errors, were considered, the ultimate bearing capacity and failure modes obtained from the experiments were in good agreement with the numerical solutions. In general, the established FE model can be used to predict the failure behavior of this type of CARALL beam. In future studies, advances numerical analysis with higher-order theories will be performed for the CARALL beams.

Acknowledgement: This research was supported by the National Natural Science Foundation of China (51708552), Natural Science Foundation of Jiangsu Province (BK20170752), and Young Elite Scientist Sponsorship. All extended support is gratefully acknowledged.

References

[1] Brittani RR, Ashley PT. Portable and rapidly deployable bridges: Historical perspective and recent technology developments. Journal of Bridge Engineering 2013; 18: 1074–1085.
[2] Zhang DD, Zhao QL, Huang YX, et al. Flexural properties of a lightweight hybrid FRP-aluminum modular space truss bridge system. Composite Structures 2014; 108(1): 600–615.
[3] Zhang DD, Lv YR, Zhao QL, et al. Development of lightweight emergency bridge using GFRP–metal composite plate-truss girder. Engineering Structures 2019; 196:109291.
[4] Zhang DD, Yuan JX, Zhao QL, et al. Static performance of a new GFRP-metal string truss bridge subjected to unsymmetrical loads. Steel and Composite Structures 2020; 35(5): 641–657.
[5] Sinmazçelik T, Avcu E, Bora MO, et al. A review: fibre metal laminates,background, bonding types and applied test methods. Materials & Design 2011; 32: 3671–3685.
[6] Ding ZR, Wang HY, Luo JM, et al. A review on forming technologies of fibre metal laminates. International Journal of Lightweight Materials and Manufacture 2020; 4(1): 110–126.
[7] Kavitha K, Vijayan R, Sathishkumar T. Fibre-metal laminates: A review of reinforcement and formability characteristics. Materials Today: Proceedings 2020; 22: 601–605.
[8] Caprino G, Iaccarino P, Lamboglia A. The effect of shear on the rigidity in the three point bending of unidirectional CFRP laminates made of T800H/3900-2. Composite Structures 2009; 88: 360–376.
[9] Dong CS, Jayawardena H, Davies IJ. Flexural properties of hybrid composites reinforced by S-2 glass and T700S carbon fibres. Composites Part B: Engineering 2012; 43: 573–581.
[10] Alhashmy HA and Nganbe M. Laminate squeeze casting of carbon fiber reinforced aluminum matrix composites. Materials & Design 2015; 67: 154–158.
[11] Xue J, Wang WX, Zhang JZ, et al. Progressive failure analysis of the fiber metal laminates based on chopped carbon fiber strands. Journal of Reinforced Plastics and Composites 2015; 34(5): 364–376.
[12] Dhaliwal GS, Newaz GM. Experimental and numerical investigation of flexural behavior of carbon fiber reinforced aluminum laminates. Journal of Reinforced Plastics and Composites 2016; 35(12): 945–956.
[13] Zakaria AZ, Shelesh-nezhad K, Chakherlou TN, et al. Effects of aluminum surface treatments on the interfacial fracture toughness of carbon-fiber aluminum laminates. Engineering Fracture Mechanics 2017; 172: 139–151.
[14] Khan F, Qayyum F, Asghar W, et al. Effect of various surface preparation techniques on the delamination properties of vacuum infused Carbon fiber reinforced aluminum laminates (CARALL): Experimentation and numerical simulation. Journal of Mechanical Science and Technology 2017; 31(11):5265–5272.
[15] Osapiuk M, Bienias J, Surowska B. Analysis of the bending and failure of fiber metal laminates based on glass and carbon fibers. Science and Engineering of Composite Materials 2018; 25(6):1095–1106.

[16] Xu RH, Huang YX, Lin Y, et al. In plane flexural behaviour and failure prediction of carbon fibre reinforced aluminium laminates. Journal of reinforced plastics and composites 2017; 36(18): 1384–1399.
[17] Lin Y, Huang YX, Huang T, et al. Characterization of progressive damage behaviour and failure mechanisms of carbon fiber reinforced aluminium laminates under three-point bending. Thin-walled Structures 2019; 135:494–506.
[18] Mao CW, Mo F, Peng YN, et al. Carbon fiber composite laminate structure and effect of clearance on riveting properties. Acta Materiae Compositae Sinica 2018; 35(12): 3280–3297 (in Chinese).
[19] Zhang YH, Yan LL, Miao MH, et al. Microstructure and mechanical properties of z-pinned carbon fiber reinforced aluminum alloy composites. Materials & Design 2015; 86: 872–877.
[20] Kim JG, Kim HC, Kwon JB, et al. Tensile behavior of aluminum/carbon fiber reinforced polymer hybrid composites at intermediate strain rates. Journal of Composite Materials 2015; 49: 1179–1193.
[21] André NM, Goushegir SM, Santos JF, et al. Friction spot joining of aluminum alloy 2024-T3 and carbon-fiber-reinforced poly (phenylene sulfide) laminate with additional PPS film interlayer: Microstructure, mechanical strength and failure mechanisms. Composites Part B: Engineering 2016; 94(1): 197–208.
[22] Lin Y, Huang YX, Huang T, et al. Open-hole tensile behavior and failure prediction of carbon fibre reinforced aluminium laminates. Polymer composites 2018; 39: 4123–4138.
[23] Botelho EC, Silva RA, Pardini LC, et al. Evaluation of adhesion of continuous fiber-epoxy composite/aluminum laminates. Journal of Adhesion Science and Technology 2004; 18: 1799–1813.
[24] Makeev A. Interlaminar shear fatigue behavior of glass/epoxy and carbon/epoxy composites [J]. Composites Science and Technology 2013; 80: 93–100.
[25] Li X, Gao W, Liu W. Post-buckling progressive damage of CFRP laminates with a large-sized elliptical cutout subjected to shear loading. Composite Structures 2015; 128: 313e321.
[26] Kumar S K, Harursampath D, Carrera E, et al. Modal analysis of delaminated plates and shells using Carrera Unified Formulation - MITC9 shell element. Mechanics of Advanced Materials and Structures 2018; 25(8): 681–697.
[27] Pagani A, Valvano S, Carrera E. Analysis of laminated composites and sandwich structures by variable-kinematic MITC9 plate elements. Journal of Sandwich Structures and Materials 2018; 20(1): 4–41.
[28] Alaimo A, Orlando C, Valvano S. An alternative approach for modal analysis of stiffened thin-walled structures with advanced plate elements. European Journal of Mechanics - A/Solids 2019; 77: 103820.
[29] Cortes P, Cantell WJ. The tensile and fatigue properties of carbon fiber-reinforced PEEK-titanium fiber-metal laminates. Journal of Reinforced Plastics and Composites 2004; 23:1615–1623.
[30] Liu PF, Chu JK, Liu YL, et al. A study on the failure mechanisms of carbon fiber/epoxy composite laminates using acoustic emission. Materials & Design 2012; 37: 228–235.
[31] Montesano J, Fawaz Z, Bougherara H. Use of infrared thermography to investigate the fatigue behavior of a carbon fiber reinforced polymer composite. Composite Structures 2013; 97: 76–83.
[32] Stoll MM, Weidenmann KA. Fatigue of fiber-metal-laminates with aluminum core, CFRP face sheets and elastomer interlayers (FMEL). International Journal of Fatigue 2018; 107: 110–118.
[33] Bienias J, Jakubczak P. Low velocity impact resistance of aluminium/carbon-epoxy fiber metal laminates. Composite Theory and Practice 2012; 12: 193–197.
[34] Wang B, Xiong J, Wang XJ, et al. Energy absorption efficiency of carbon fiber reinforced polymer laminates under high velocity impact. Materials & Design 2013; 50: 140–148.
[35] Moriniere FD, Alderliesten RC, Sadighi M, et al. An intergrated study on the low-velocity impact response of the GLARE fiber-metal laminate. Composite Structures 2013; 100: 89–103.
[36] Bienias J, Jakubczak P, Surowska B, et al. Low-energy impact behaviour and damage characterization of carbon fibre reinforced polymer and aluminium hybrid laminates. Archives of Civil and Mechanical Engineering 2015; 15: 925–932.
[37] Yu GC, Wu LZ, Ma L, et al. Low velocity impact of carbon fiber aluminum laminates. Composite Structures 2015; 119: 757–766.
[38] Jaroslaw B, Barbara S, Patryk J. The comparison of low-velocity impact resistance of aluminum/carbon and glass fiber metal laminates. Polymer Composites 2016; 37: 1056–1063.
[39] Kaboglu C, Mohagheghian I, Zhou J, et al. High-velocity impact deformation and perforation of fibre metal laminates. Journal of Materials Science 2017; 534: 4209–4228.
[40] Dhaliwal GS, Newaz GM. Compression after impact characteristics of carbon fiber reinforced aluminum laminates. Composite Structures 2017; 160: 1212–1224.
[41] Shen Y, Ke J, Wu ZZ. Energy-absorbing characteristics of carbon fiber reinforced polymer composite-AL square tubes with different braiding angles. Acta Materiae Compositae Sinica 2020; 37(3): 591–600 (in Chinese).
[42] Shin DK, Kim HC, Lee JJ. Numerical analysis of the damage behavior of an aluminum/CFRP hybrid beam under three point bending. Composites Part B: Engineering 2014; 56: 397–407.
[43] Dimitri R, Trullo M, Zavarise G, et al. A consistency assessment of coupled cohesive zone models for mixed-mode debonding problems. Frattura Ed Integrità Strutturale 2014; 8(29):266–283.
[44] Dimitri R , Trullo M , Lorenzis LD , et al. Coupled cohesive zone models for mixed-mode fracture: A comparative study. Engineering Fracture Mechanics 2015; 148(1):145–179.
[45] Ridha M, Wang C H, Chen B Y, et al. Modelling complex progressive failure in notched composite laminates with varying sizes and stacking sequences. Composites Part A: Applied Science and Manufacturing 2014; 58: 16–23.
[46] Shin D K, Kim H C, Lee J J. Numerical analysis of the damage behavior of an aluminum/CFRP hybrid beam under three point bending. Composites Part B: Engineering 2014; 56:397–407.